Efficacy of treating segmental bone defects through endochondral ossification: 3D printed designs and bone metabolic activities

Kenji Hara [a,b], Endre Hellem [a], Shuntaro Yamada [a], Kemal Sariibrahimoglu [a], Anders Mølster [c], Nils R. Gjerdet [d], Sølve Hellem [a], Kamal Mustafa [a], Mohammed A. Yassin [a,*]

[a] Centre of Translational Oral Research (TOR) – Tissue Engineering Group, Department of Clinical Dentistry, University of Bergen, Bergen, Norway
[b] Department of Oral and Maxillofacial Surgery, Fujieda Heisei Memorial Hospital, Japan
[c] Department of Clinical Medicine, University of Bergen, Bergen, Norway
[d] Department of Clinical Dentistry, Faculty of Medicine, University of Bergen, Bergen, Norway

ARTICLE INFO

ABSTRACT

Three-dimensional printing (3D printing) is a promising technique for producing scaffolds for bone tissue engineering applications. Porous scaffolds can be printed directly, and the design, shape and porosity can be controlled. 3D synthetic biodegradable polymeric scaffolds intended for in situ bone regeneration must meet stringent criteria, primarily appropriate mechanical properties, good 3D design, adequate biocompatibility and the ability to enhance bone formation. In this study, healing of critical-sized (5 mm) femur defects of rats was enhanced by implanting two different designs of 3D printed poly(L-lactide-co-ε-caprolactone) (poly(LA-co-CL)) scaffolds seeded with rat bone marrow mesenchymal stem cells (rBMSC), which had been pre-differentiated *in vitro* into cartilage-forming chondrocytes. Depending on the design, the scaffolds had an interconnected porous structure of 300–500 μm and porosity of 50–65%. According to a computational simulation, the internal force distribution was consistent with scaffold designs and comparable between the two designs. Moreover, the defects treated with 3D-printed scaffolds seeded with chondrocyte-like cells exhibited significantly increased bone formation up to 15 weeks compared with empty defects. In all experimental animals, bone metabolic activity was monitored by positron emission tomography 1, 3, 5, 7, 11 and 14 weeks after surgery. This demonstrated a time-dependent relationship between scaffold design and metabolic activity. This confirmed that successful regeneration was highly reproducible. The *in vitro* and *in vivo* data indicated that the experimental setups had promising outcomes and could facilitate new bone formation through endochondral ossification.

1. Introduction

Bone is a vascularized, dynamic tissue with great regenerative capability. In bone tissue engineering, successful simulation of bone design requires an understanding of the unique functional biophysical properties and features of natural bone. Bone tissue consists of connective tissue with mineralized extracellular matrix (ECM). Only under certain circumstances does it have the capacity for full regeneration of simple fractures or small defects. In long bone fractures, at least 10% do not heal [1,2]. For large bone defects, autografts promote faster union and are considered to be the most effective treatment [3]. However, due to the lack of suitable autologous bone and the complication of donor site morbidity, the routine use of autografts is restricted [4,5]. A potential

treatment alternative is bone tissue engineering, which involves an interaction of stem cells, biomaterials and bone active growth factors to regenerate bone tissue [6]. Bone development and fracture repair can occur either through intramembranous or endochondral ossification [7]. In tissue engineering, the intramembranous process is the most widely used regenerative strategy: bone ECM is directly created *in vitro* and later implanted *in vivo* [8]. In contrast, in endochondral ossification, mesenchymal stem cell (MSC) differentiate into chondrocytes, which form a cartilage template [9]. Within this template, chondrocytes secrete cytokines and growth factors such as vascular endothelial growth factor and enzymes such as alkaline phosphatase (ALP). Together these factors stimulate building vascular networks with hierarchical architectures and formation of the cartilage template, which is subsequently resorbed by

---

osteoclasts and replaced by bone [9,10]. Chondrocytes can survive in environments with low nutrient, however, some limitations for instance low isolation productivity, poor proliferation ability and fast phenotypic shift were found. The invention and discovery of MSC from different sources offered attractive substitutes to chondrocytes which are useful alternative harvest sites for cells for *in vivo* implantation [11,12].

In endochondral ossification, bone marrow-derived mesenchymal stromal cells (BMSC) have been a common cell source [13]. In induction of chondrogenic differentiation by using effective morphogens such as bone morphogenetic proteins, BMSC characteristically acquire a hypertrophic phenotype [14]. The *in vivo* implantation of this phenotype destabilizes the cartilage tissue, which tends to undergo endochondral ossification and progression to bone formation [15]. Moreover, bone tissue regeneration through endochondral ossification using BMSC has been well verified using ectopic [16] or orthotropic models [17,18]. BMSC require a pre-culture time of 2–6 weeks in chondrogenic media [14]. These characteristics, combined with the robustness and efficiency of this approach, indicate that endochondral bone regeneration warrants further investigation for clinical translation [19–22].

In bone tissue engineering, the scaffolding should provide a conductive microenvironment for the seeded cells. A recent trend, intended to enhance bone regeneration, is to customize scaffolds with pre-designed models and functions [23,24]. Various fabrication methods have been developed to assemble the 3D construct, for example phase separation, freeze-drying, salt leaching, gas foaming, particle sintering, and solid free-form fabrication (SFF) [25]. By comparison, 3D printing has many advantages [25], producing customized 3D scaffolds with unique architecture and properties necessary for advanced biomedical applications [26]. To simulate the properties of bone, a number of structural parameters should be tailored, such as surface area to volume ratio, porosity, pore size and interconnectivity [27]. It has been shown that pore shape, size and interconnections are crucial for the diffusion of nutrients, progenitor cell differentiation, vascular infiltration, biomaterial degradation and bone regeneration [28]. Furthermore, a balance between porosity and strength is essential, to ensure that the 3D scaffold can withstand the loading stresses at the defect site during and after surgery [29].

Among 3D printing methods, the direct melt extrusion-based process has been shown to be appropriate for aliphatic polyesters [30,31]. Fundamental to successful 3D scaffold fabrication is the selection of appropriate raw materials. The raw materials are major determinants of the final properties of the biomaterial, such as biocompatibility, biodegradability, and mechanical properties. Poly(ʟ-lactide-co-ε-caprolactone) (poly (LA-co-CL)) meets these criteria [32–34]. Salt-leaching and 3DP methods were used to produce poly(LLA-co-CL) scaffolds with 25 mol % ε-caprolactone as good candidates for bone regeneration [35,36]. By copolymerization of poly(ʟ-lactide) with poly(ε-caprolactone) the scaffolds showed gradual degradation within 91 days of the experimental period [37]. Moreover, it possesses an appropriate structure, which can be modified to improve the functional properties of regenerated bone tissues [32–34]. Recently we reported that 3D printing of poly (LA-co-CL) scaffolds were printable at higher molecular weights and formed lower molecular weight compounds over the course of printing, which do not affect the overall molecular weight [31].

The design of scaffolds is crucial for bone tissue engineering because it allows the formation of new bone and capillaries. After implantation, 3D porous scaffolds must provide mechanical support to the damaged hard tissue in a manner similar to natural healing. Yet, it is difficult to predict the amount of new bone generated by pre-designed scaffolds that simulate detectable size and shape. As a result, the current study sought to answer the question "How can the design of the scaffold affect bone metabolic activities and bone formation?". We used two rigorous designs, and a biodegradable synthetic copolymer that can be printed using a high resolution bioprinter to answer that question. In this study, finite element analysis (FEA), positron emission tomography/computed tomography (PET/CT), long bone defect model, micro-computed tomography (CT), and histology were used to evaluate the effect of 3D-printed scaffolds on their mechanics, bone metabolic activities, and bone regeneration capacity.

2. Materials and methods

2.1. Study design

Fig. 1 shows the design of the current study. In brief, from the left femur of a 12-week-old Lewis rat (inbred rats), a full thickness segment 5
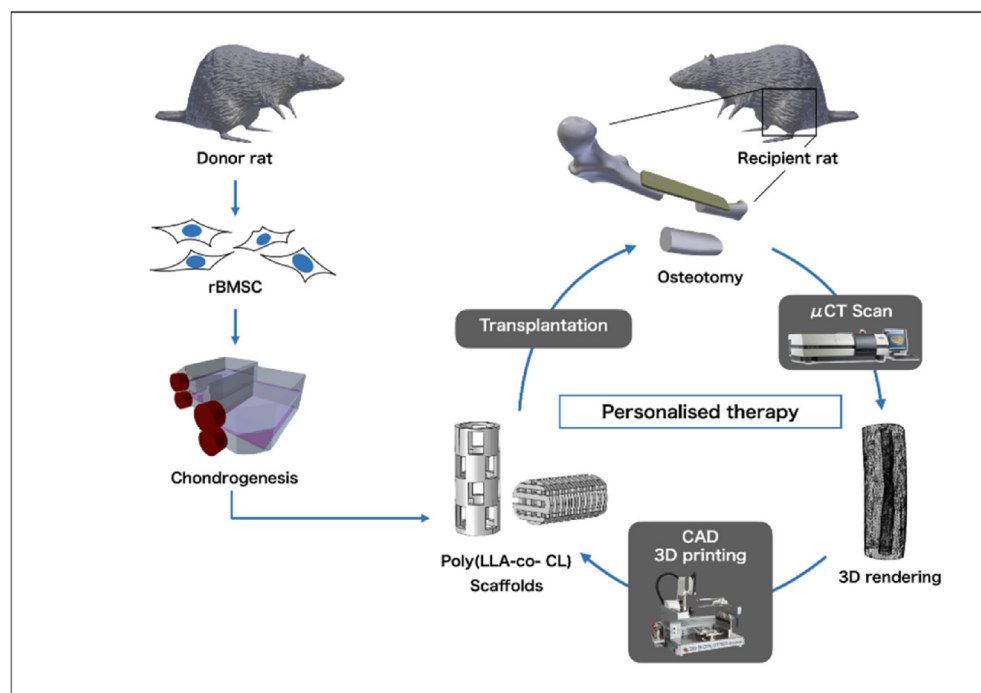

Fig. 1. Schematic illustration of the study design. From a 12-week-old Lewis rat, a full thickness 5 mm segment was taken from the mid-femoral diaphysis. The segment was scanned by μ-CT and an STL file was produced. Using the STL file, a 3D-bioplotter was used to fabricate two different designs. rBMSC were seeded onto the printed scaffolds and the constructs were subjected to sequential chondrogenesis in chondrogenic medium for 21 days. The constructs were implanted into the defects for a follow-up period of up to 15 weeks. Empty defects were used as control.
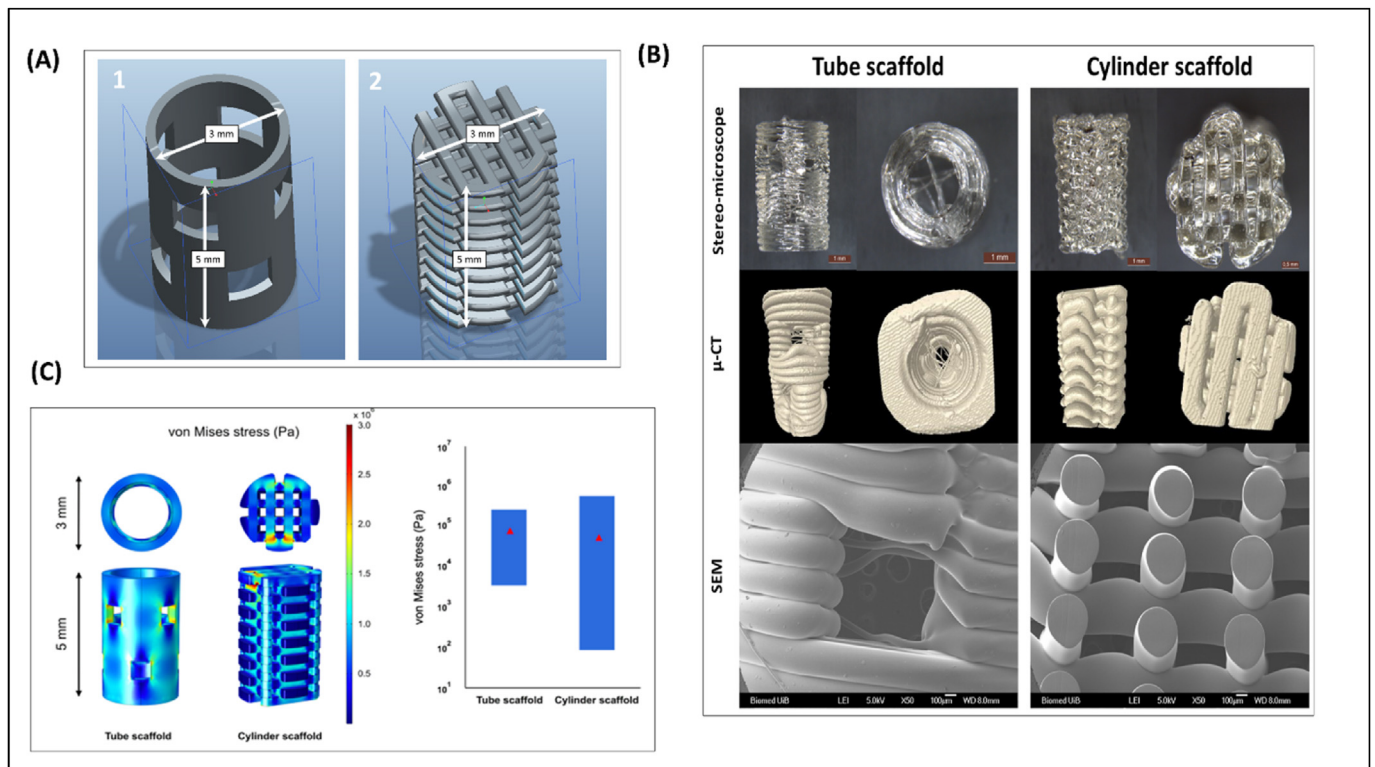
Fig. 2. Poly(LA-co-CL) scaffolds. (A) The two designs: 1. The Tube scaffold, with a simulated medullary canal, has pores on the walls to stimulate vascularization. and 2. Cylinder scaffold, fabricated by 0/90° lay-down pattern, (B) Stereo-microscope, μ-CT and SEM images of the printed scaffolds. (C) In-silico simulation model for evaluation of mechanical strength of the scaffolds. Top and lateral schematic images of stress distribution within tube and cylinder scaffolds. Stress is accumulated in the area of pores in the tube scaffold and in the first and second layers in the cylinder scaffold. Calculated value of von Mises stress (Pa). The bars show the range of stress, from minimum to maximum, in each scaffold (Red triangle: average stress). (For interpretation of the references to color/colour in this figure legend, the reader is referred to the Web version of this article.)

mm in length was cut from the mid-femoral diaphysis and scanned by micro-computed tomography (μ-CT). From the axial cuts, the three-dimensional contour of the femur was reconstructed using NRcon software, to create a simple stereolithography file (STL) in CTAnalyser software. Using these anatomic dimensions, a polymeric scaffold was fabricated via layer-by layer deposition using a three-dimensional printing system, 3D-bioplotter (EnvisionTEC, Germany). Two different designs were fabricated: tube-shaped or cylinder-shaped. The scaffolds were seeded with rBMSC and subjected to chondrogenic differentiation, before being inserted into the 5-mm defects. The follow-up time was 15 weeks and empty defects were used as control.

2.2. Synthesis of the copolymer

The composite consisted of poly(ʟ-lactide-co-ε-caprolactone) (PLA/PCL, ratio 70:30) by weight. Poly(LA-co-CL) was synthesized by ring opening polymerization reaction with following protocol at 110 °C, according to a previously described method [38]. Briefly, ε-Caprolactone (CL, Sigma-Aldrich, Germany) was dried with CaH_2 overnight and purified by distillation at 80 °C. L-La (LLA, Boehringer Ingelheim, Germany) was recrystallized three times and dried under vacuum. Ethylene glycol and $Sn(Oct)_2$ served as initiator and catalyst respectively. The monomer to catalyst ratio was set to 10000:1. The synthesis was carried out in a 250-mL round bottom flask under mechanical stirring in a dry nitrogen atmosphere. The copolymer was precipitated in hexane/methanol and repeatedly washed with water to remove the residual monomer and metal ions.

2.3. Scaffolds designs

The 3D printing processes begin with a CAD taken from bone structures. 2D slices acquired from μ-CT imaging scanning were compiled and stacked on top of one another to form a 3D structure. A 3D virtual model in STL file format was then transferred to the 3D-Bioplotter® (EnvisionTEC, Germany) and scaffold fabrication began.

For bone regeneration, it is imperative to grow tissue similar to that of the native tissue. For this purpose, two scaffold designs were developed, closely resembling the structure of native bone (Fig. 2). The tailor-made scaffolds were prepared using the 3D Bioplotter as follows:

I. The tube scaffold is hollow, with pores on the walls to stimulate vascularization.
II. The cylindrical scaffold is designed by 0/90° lay-down pattern.

2.4. 3D printing parameters

The cartridge was pre-heated to a specified temperature and polymer was then added. After an interval, the temperature was changed to an optimized printing temperature: for poly(LA-co-CL), the pre-heating temperature used was 190 °C and this temperature was maintained for 5 min before printing at 175 °C.

Two different designs and shapes were printed to simulate long bone anatomy. Briefly, a 3D CAD model of each design was constructed using Magics software (EnvisionTEC). Following the instructions of the manufacturer (EnvisionTEC GmbH, Germany), the CAD models were sliced into different layers with an 80% slicing thickness of the inner

diameter of the needle (ID) prior to printing. A slicing thickness of 0.32 mm (Bioplotter [RP], EnvisionTEC) was used for the 0.4 mm ID stainless steel needle scaffolds, printed onto double-sided tape for better adhesion.

After printing, the scaffolds were sterilized in an inert atmosphere using electron beam radiation at a dose of 2.5 Mrad from a pulsed electron accelerator (Mikrotron, Acceleratorteknik, Stockholm, Sweden) at 6.5 MeV.

2.5. Characterization of 3D printed scaffolds

A μ-CT imaging system (SkyScan 1172, Bruker, Kontich, Belgium) was used to quantify scaffold volume (mm3), surface area (mm2), porosity (vol%) and surface to volume ratio. Each scaffold was scanned at 40 kV, 250 mA without a filter. NRecon and CTan software (SkyScan) were used for volumetric reconstruction and image analysis. A cylindrical volume of interest (VOI) 4.0 mm in diameter and 5.0 mm in height was selected to remove the edge of effect. The following equation was applied to calculate porosity, in order to confirm the value from the μ-CT:

Porosity $(\%) = (volume\ of\ interest$

$- volume\ of\ scaffold\ object) / volume\ of\ interest \times 100$

Printed poly(LLA-co-CL) scaffolds were examined by scanning electron microscopy (SEM) (JSM-7400F, Joel, Tokyo, Japan). Samples were mounted on aluminum pin stubs using conductive self-adhesive carbon labels and sputter-coated with a 10 nm coating of gold-palladium. The samples were examined at magnifications ranging from $50\times$ to 100x, at an acceleration voltage of 5 kV.

2.6. In silico evaluation of different scaffold designs

In silico simulation was undertaken to evaluate the mechanical applicability of the experimental scaffolds for *in vivo* transplantation, using the COMSOL Multiphysics® software ver. 5.4 with the solid mechanics module (COMSOL AB, Stockholm, Sweden). The geometry of the 3D-printed tube and cylinder scaffolds was reproduced and meshed, and material properties, including Young's modulus and density, were determined as previously described [39,40]. In the simulation, a compressive force of 200 g was applied to the top surface while the bottom surface was defined as a fixed constraint. The internal stress was expressed as von Mises stress.

2.7. Isolation and expansion of rat mesenchymal stem cells

Rat bone marrow mesenchymal stem cells (rBMSC) were obtained from 5 male Lewis rats. The rats were housed under uniform conditions for at least 1 week before the experiment, then euthanized by an overdose of carbon dioxide (CO_2) inhalation. Briefly, extracted femurs were washed in Dulbecco's phosphate-buffered saline without calcium and magnesium (PBS), with 3% of antibiotic-antimycotic (GibcoTM, Invitrogen), and muscles and extra-ostial tissue were trimmed. Both ends of the femur were removed and bone marrow was collected by flushing out with complete medium, using a 25-gauge needle attached to a 10 mL syringe. Complete medium consisted of minimum essential medium (αMEM, InvitrogenTM, Carlsbad, California, USA) supplemented with 15% fetal bovine serum (FBS), 100 U/mL penicillin and 100 μg/mL streptomycin (Invitrogen). The cells from bone were plated in 15 mL complete medium in a T-75 flask (NUNC A/S, Roskilde, Denmark) at 37 °C, 5% CO_2. After 48 h of culture, the medium and non-adherent cells were removed by washing with PBS, and fresh medium was added. The adherent cells (passage 0) were washed, and fresh medium was added every 3–4 days for a week. After one week, the cells were washed with PBS and exposed to 2 mL 0.25% trypsin/EDTA for 5 min at 37 °C.

Suspension of the cells (passage 1) from the 1 T-75 flask was replaced in 25 mL of complete medium in a T-175 flask. Culture medium was replaced every 3–4 days for a week. The cells of further passages were replated at 8.5×103 cells/cm2 for all subsequent passages (passages 2–4). The study was approved by the Norwegian Animal Research Authority and conducted according to the European Convention for the Protection of Vertebrates Used for Scientific Purposes (ID6383, August 18, 2014).

For verification of sub-cultured cells as stem cells, rBMSC were authenticated as MSC, based on adherence to plastic in normal culture conditions, multilineage differentiation potential and flow cytometry for stem cell surface markers [41]. To validate the multipotency of rBMSC, their ability for differentiation into chondrocytes, adipocytes and osteoblasts was analyzed. For chondrogenic differentiation, the cells were cultured in 3D pellet using chondrogenic differentiation medium (CCM000/CCM020, R&D Systems, USA) following manufacturer's protocol. After 21 days of incubation, the chondrogenic pellets were embedded in Tissue-Tek® O.C.T.™ Compound (4583, Sakura, Netherlands) and sectioned into 7 μm thick slices at −18 °C using a cryostat (MNT, SLEE, Germany). The samples were stained with 1% Alcian Blue (pH 2.5; A5268, Sigma-Aldrich, USA) dissolved in acetic acid for 30 min at RT and washed five times with Milli-Q water. For osteogenic differentiation, rBMSC were seeded and incubated in α-MEM supplemented with 1% penicillin and streptomycin, 10% FBS, 173 μM ʟ-ascorbic acid (A8960; Sigma-Aldrich, USA), 10 nM Dexamethasone (D4902; Sigma-Aldrich, USA) and 10 mM β-Glycerophosphate (G9422; Sigma-Aldrich, USA) up to 21 days. To assess deposition of mineral, the cells were stained with 0.1% Alizarin red S for 20 min, followed by washing 5 times with Milli-Q water. For adipogenic differentiation, rBMSC were incubated in α-MEM supplemented with 1% Penicillin-Streptomycin, 10% FBS, 100 nM Dexamethasone, 10 μg/ml Insulin (I9278-5 ML; Sigma-Aldrich, USA), 0.2 mM Indomethacin (17378 -5G; Sigma-Aldrich, USA) and 0.5 mM 3-Isobutyl-1-methylxanthine (I5879-250 MG; Sigma-Aldrich, USA) for 14 days. To identify lipids, the cells were stained with 0.5% Oil Red O (CAT NO) in isopropanol for 30 min, followed by washing 3 times with PBS. The cell nuclei were counterstained with Hematoxylin solution (GHS3-50 ml, Sigma-Aldrich, USA) for 5 min and washed three times with PBS.

For antigen surface detection of stem cell, flow cytometry was used. In brief, rBMSC at passage 3 were trypzinised and resuspended in blocking buffer composed of staining buffer (BUF0730, Bio Rad) with 0.5% BSA (37,525, ThermoScientific) and 2% FBS. Primary antibodies used were anti-CD44H IgG2aκ antibody (1:100; 203901, BioLegend, USA), anti-CD73 IgG1κ antibody (1:100; 551123, BD Pharmingen, USA), PE anti-CD90 IgG1κ antibody (1:100; 551401, BD bioscience, USA), FITC anti-CD34 IgG2aκ antibody (1:100; 11-0341-82, eBioscience, USA), PE anti-CD45 IgG1κantibody (1:100; 202207, BioLegend, USA) and PE anti-CD79 IgG1κ antibody (1:100; 12-0792-41, eBioscience, USA). The data of the stained cells were captured by AccuriC6 (BD Biosciences, USA) and analyzed using FlowJo software version 10.6.2 (Becton, Dickinson & Company, USA).

2.8. Preparing a cell-scaffold construct

To determine the initial cell seeding efficiency, 2.0 million cells with 100 μL of complete medium were dropped onto the top of the scaffolds standing upright in a 24-well plate. Samples were incubated at 37 °C, 5% CO_2 for 1.5 h. The samples were then inverted and incubated for another 1.5 h. Cell suspension around the bottom of the scaffold was collected and re-dropped onto scaffolds when the samples were inverted. In all, the samples were cultured for 3 h, each well receiving 500 μl of complete medium. After 24 h, unattached remaining cells in the medium were counted using Countess® (Invitrogen) (duplicate measurement, n = 4).

The cell loading efficiency was determined by the following formula

(Vicryl 4–0, Ethicon, Belgium).

$$\text{Initial cell seeding efficiency} = \frac{(2.0\ million - The\ total\ number\ of\ unattached\ cells\ per\ well)}{2.0\ million} \times 100$$

Two million rBMSC were seeded onto scaffolds and allowed to attach for 24 h. For chondrogenic differentiation, cell-scaffold constructs were transferred into a chondrogenic differentiation medium, StemPro®Chondrogenesis Differentiation Kit (Invitrogen), and cultured for 21 days. The differentiation medium was changed every 3 days.

To confirm the chondrogenic differentiation of rBMSC after 21 days, SEM imagining, and quantitative reverse transcription polymerase chain reaction (RT-qPCR) were applied. For SEM, the medium was replaced with 2.5% glutaraldehyde in a-MEM without serum and fixed for 30 min. Then, samples were fixed in 2.5% glutaraldehyde in 0.1 M sodium cacodylate pH 7.2 and treated with 1% osmium tetroxide in distilled water for 1 h, followed by dehydration through a graded series of ethanol solutions, critical point-dried (using CO_2 as transitional fluid and the specimens mounted on aluminum holders), and sputter-coated with a 10 nm conducting layer of gold platinum. Finally, the samples were examined by SEM (Jeol JSM 7400F, Tokyo, Japan) using a voltage of 10 kVhe.

For RT-qPCR were snap-frozen in liquid nitrogen on 21 days and stored at − 80 °C until processed. Total RNA was extracted using a Maxwell® 16 Cell LEV Total RNA Purification Kit (AS1280; Promega, USA) in accordance with the manufacturer's protocol. Subsequently, reverse transcription was performed using a Transcription Kit (4368814; Applied Biosystems, USA). RT-qPCR was conducted with the StepOne™ real-time PCR system (4453320, Applied Biosystems, USA). The primers used were Aggrecan (agg) F 5′-GGCCTTCCCTCTGGATTTAG-3′ R 5′-CCGCACTACTGTCCAAC-3′ and Collagen II (col II) F 5′-AGGGGTAC-CAGGTTCTC CATC-3′ R 5′-CTGCTCATCGCCGCGGTCCGA-3′ as reported before [42]. Relative expression of each mRNA was calculated with the $^{\Delta\Delta}$Ct method normalized by GAPDH (n = 5).

2.9. In vivo study

2.9.1. Surgical procedures

The animal procedures were conducted in accordance with Norwegian and EU animal safety regulations. The number of animals to be used in the experiments was reduced to the minimum required (n = 8). The rats were anaesthetized with sevoflurane. Sevoflurane was evaporated up to MAC 7–8% for induction, and MAC 3–4% inhalant for maintaining anesthesia during an operation, with an oxygen flow rate of 300–400 mL/min. The surgical site on the left leg was shaved and washed with iodide. A lateral approach was made, by skin incision between the greater trochanter and the knee joint. Before incision, Temgesic was injected intraperitoneally for analgesia, at a concentration of 0.1 mg/kg. The intermuscular plane between the vastus lateralis and the biceps femoris muscles was separated. The periosteum of the femur was incised. The plate was fitted to the middle of the femur and fixed to the surface with gentle force from a pair of forceps. After predrilling the holes using a 0.79 mm drill bit, the plate was attached to the femur with six 0.8-mm bicortical titanium screws. A 5 mm defect was created by using Piezotome Solo (Acteon). After removal of the bone segment, the defect was rinsed with sterile saline. Defects were either left empty (controls) or implanted with one of the two types of cell-scaffold constructs (experimental groups). The scaffolds were secured in place in the defect by ligating them to the plate with two absorbable sutures (Vicryl 4–0, Ethicon, Belgium). The wound was closed with absorbable sutures

2.9.2. In vivo imaging

Positron emission tomography/computed tomography (PET/CT) imaging was carried out one week after surgery, and then every two weeks, starting from 3 weeks, up to 15 weeks postoperatively. ^{18F}-sodium fluoride (^{18F}–NaF) PET/CT data were acquired just after and 45 min after injecting ∼ 15 MBq/rat of ^{18F}–NaF in 0.9% NaCl (500 μL/rat) from cannulation of a tail vein, with a nanoScan small animal PET/CT scanner (Mediso Medical Imaging System, Budapest, Hungary). PET emission scans were acquired for 10 min just after injection of 18F–NaF, followed by CT acquisitions for anatomic correlation (spatial resolution; 250 μm, 70 kV, exposure time: 300 ms, projections: 480, binning: 1:4). After CT acquisitions for anatomic correlation, high resolution CT data were acquired for CT analysis (spatial resolution: 60 μm, 70 kV, exposure time: 300 ms, projections: 720, binning: 1:1).

2.9.3. Analysis of the PET/CT images

Nucline software (Mediso Medical Imaging System, Budapest, Hungary) was used for PET data reconstruction with correction for attenuation based on CT data. Inter View Fusion software (Mediso) was used for co-registration of PET and CT data, quantification of standard uptake values in as interesting area, and three dimensionally visualization.

2.9.4. Ex vivo radiological monitoring

New bone formation during the healing process was observed by ex-vivo μ-CT scanning. The harvested femora were analyzed using a high resolution μ-CT system (Skyscan 1172, Skyscan, Belgium). Scans were taken at 80 kVp, with a 0.5 mm aluminium filter and a pixel size of 10 μm. Scans were reconstructed volumetrically to provide 3D representations of the bone defect, and analyses were undertaken using NRecon Reconstruction and CTAn softwares. Bone volume and bone surface to volume ratio within the defect were calculated. The volume of interest (VOI) was centered on the bone defect.

2.10. Histology

After μ-CT, bone samples were fixed in 4% paraformaldehyde for 24 h, decalcified for 4 weeks in EDTA solution, dehydrated through an ethanol series, cleaned by xylene and embedded in paraffin. The paraffin-embedded samples were sliced into 5 μm sections (Leica RM2235, Germany). After staining with hematoxylin and eosin (H&E stain), optical microscopy was used to detect bone regeneration.

Table 1
Topology and 3D analysis of the 3D printed scaffolds calculated from μ-CT analysis.

	Tube scaffold	Cylinder scaffold
Scaffold volume (mm³)	25.07 ± 2.3	41.72 ± 1.4
Surface area (mm²)	231.95 ± 5.3	273.46 ± 7.2
Porosity (%)	66.30 ± 2.1*	53.14 ± 2.2
Surface density (/mm)	5.26 ± 1.2	6.55 ± 1.1

2.11. Statistical analysis

All data were presented as mean ± SD. One-way ANOVA with a Tukey post-hoc test was used for inter-group statistical analysis, unless indicated otherwise. P < 0.05 was considered significant.

3. Results and discussion

3.1. Preparation and characterization of 3DP scaffolds

The first step was to establish a method for constructing 3DP polymeric scaffolds of two different designs, with an internal architecture simulating that of the long bone. μ-CT analysis was used to characterize the printed scaffolds (Table 1). The porosity of the Tube scaffold was significantly higher than that of the Cylinder scaffold. The pore sizes of the scaffolds ranged from 300 to 500 μm. The fabrication processes and printing parameters were intended to deliver poly(LA-co-CL) scaffolds which were effective stem cell carriers.

The design of the 3D printed scaffolds is shown in Fig. 2A. Tube scaffolds were hollow, similar to cortical bone structure, including simulation of the medullary canal, with 500 μm pores on the surface. In the Cylinder scaffold, the orientation angles of the stacked layers were 0 and 90°. Fig. 2B shows the detailed inner and outer architecture of the scaffolds, as observed by optical microscopy, μ-CT and SEM.

Recent developments in temporo-spatial specific 3D printing techniques show great promise as a reliable approach to customizing the physical structure of a polymeric scaffold [43]. A direct extrusion-based 3D printer was used to print poly(LA-co-CL) inserts, intended for regeneration of segmental defects in rats. The scaffolds were printed with reasonable reliability, according to a predesigned 3D structure model [44,45].

It is widely accepted that for a bone defect implant, a scaffold should have a micro-pore size greater than 300 μm and a porosity of over 50%. These dimensions offer good potential for vascularization and the resultant direct reparative osteogenesis [46]. Thus, the porosity of the present scaffolds is acceptable for potential application in bone regeneration.

The computerized simulation showed internal force distribution in accordance with the scaffold designs (Fig. 2C). In the Tube scaffold, compressive stress was more evenly distributed, except in the area of the pores, where greater stress accumulated. The minimum, maximum and average stresses were 3.51×10^1 kPa, 2.46×10^3 kPa and 8.65×10^2 kPa, respectively. In the Cylinder scaffold, the internal stress was less balanced, with accumulation of greater internal stress in the first and second layers. However, the minimum, maximum and average stresses were 0.87 kPa, 5.86×10^3 kPa and 5.67×10^2 kPa, indicating that the average and maximum stresses were comparable with those in the Tube scaffold.

During the post-transplantation healing period, normal physical activity resumed. Although the bony defects were supported with splints, it is anticipated that transplanted scaffolds will be subjected to loading. They therefore require adequate mechanical properties. To evaluate the therapeutic applicability of our scaffolds, we conducted in-silico simulation, applying the finite element method. In our simulation, the geometry and basic mechanical properties were reproduced, and 200 g, the average weight of the recipient rats, was loaded onto the scaffolds. Despite the difference in stress distribution between the two designs, the average stress in both scaffolds was equivalent and, more importantly, the maximum stress was lower than the breaking point of poly(LA-co-CL), approximately $1–2 \times 10^4$ kPa [39,40]. On the basis of these results, it was concluded that the two different scaffold designs were applicable for *in vivo* transplantation.

Stress and strain stimulate bone regeneration in long bones [47]. This factor needs further consideration with respect to application of 3D-printed scaffolds in large defects, as used in the present experiments. A computer model for bone regeneration has shown that optimized initial mechanical conditions within a bone scaffold do not guarantee that the predicted ideal bone regeneration will be achieved. Some scaffold designs performed remarkably well immediately after implantation, but after 60 days bone formation was low [47]. Our results, however, demonstrate that mechanical properties computed immediately after 3DP scaffold implantation can reliably serve as proxy indicators of clinically successful bone regeneration. This may be a result of the fixation technique stabilizing the 3DP scaffolds within the defect. Stability of bone-scaffold mechanical environment up to 15 weeks post-operatively helped to foster bone regeneration.

It has been reported that a suitably interconnected structure as well as adequate mechanical properties are critical for a 3D biodegradable porous polymeric scaffold to support the repair of defective bone tissue [48,49]. Degradable polymeric biomaterials have inherently weak mechanical properties, and this is exacerbated by the need for scaffold porosity. This is difficult to reconcile with reports in some earlier studies that 3D porous biodegradable polymeric scaffolds had adequate mechanical properties [46,50]. It has been suggested that cartilaginous engineered constructs can continue to function mechanically in load-bearing bone sites of small animals [51]. 3D printing allows precise control of the structural mechanical properties of the engineered construct. In the present investigation, combining the good mechanical properties of poly(LA-co-CL) and high heat extrusion 3D printing with a high concentration of polymeric ink, we achieved highly interconnected 3D scaffolds with adequate mechanical properties. The results confirm that this is a promising approach to the manufacture of scaffolds for bone regeneration, with potential biomedical applications.

3.2. Characterization and chondrogenic differentiation of rBMSC in vitro

It was confirmed that cells from the bone marrow of five 4-week-old male Lewis rats were mesenchymal stem cells. During the initial days of incubation, attachment to the culture flasks was sparse and the cells exhibited a fibroblast-like, spindle-shaped morphology. The multipotency of rBMSC and their ability to differentiate into chondrocytes, osteoblasts and adipocytes was confirmed (Fig. 3A). Further, flow cytometry verified that the cells expressed stem cell markers, including CD44H, CD73, and CD90. There was no expression of hematopoietic markers, such as CD34, CD45 and CD79 (Fig. 3B).

The initial efficiency of cell attachment was assessed after 24-h of culture on scaffolds (Fig. 3. C). Seeding efficiency on the Tube and Cylinder pore scaffolds was 77.7% and 73.0%, respectively. Cell seeding efficiency plays an important role in the success of engineered constructs and is influenced mainly by surface properties, porosity and scaffold architecture [52]. The suitable scaffolds for bone tissue regeneration must be highly interconnected porous templates. It has been reported that increased porosity and pore size typically consequence in high surface area/volume ratio that favoring cell adhesion to the constructs leading to promote bone regeneration [53]. Compared with conventional techniques for scaffold production, such as the salt leach technique, seeding efficiency is higher in the 3D printing method [32]. The 3D Bioplotter uses consumptions compressed air to print the poly(LA-co-CL) in addition to high pressure which lead to increase the oxygen with the polymer when printing at high temperature, resulting in thermal-oxidative degradation of the polymer [54]. This might have led to a change in surface properties of the scaffolds which enhanced the seeding efficiency.

For culture of the chondrocytic phenotype, rBMSC were seeded onto 3D printed Tube and Cylinder poly(LA-co-CL) scaffolds and cultured in a chondrogenic differentiation medium for 21 days. SEM images after 21 days' induction showed that the seeded cells on the scaffolds formed complex cells like chondrocytes (the whole scaffold is covered with a gel-like deposit (Fig. 3. D). It is confirmed by the overall significant upregulation of agg and col II genes expression in chondrogenic medium (p < 0.001) after 21 days as shown in (Fig. 3. E). It is necessary for the transition to chondrocytes, which express and deposit cartilage-specific
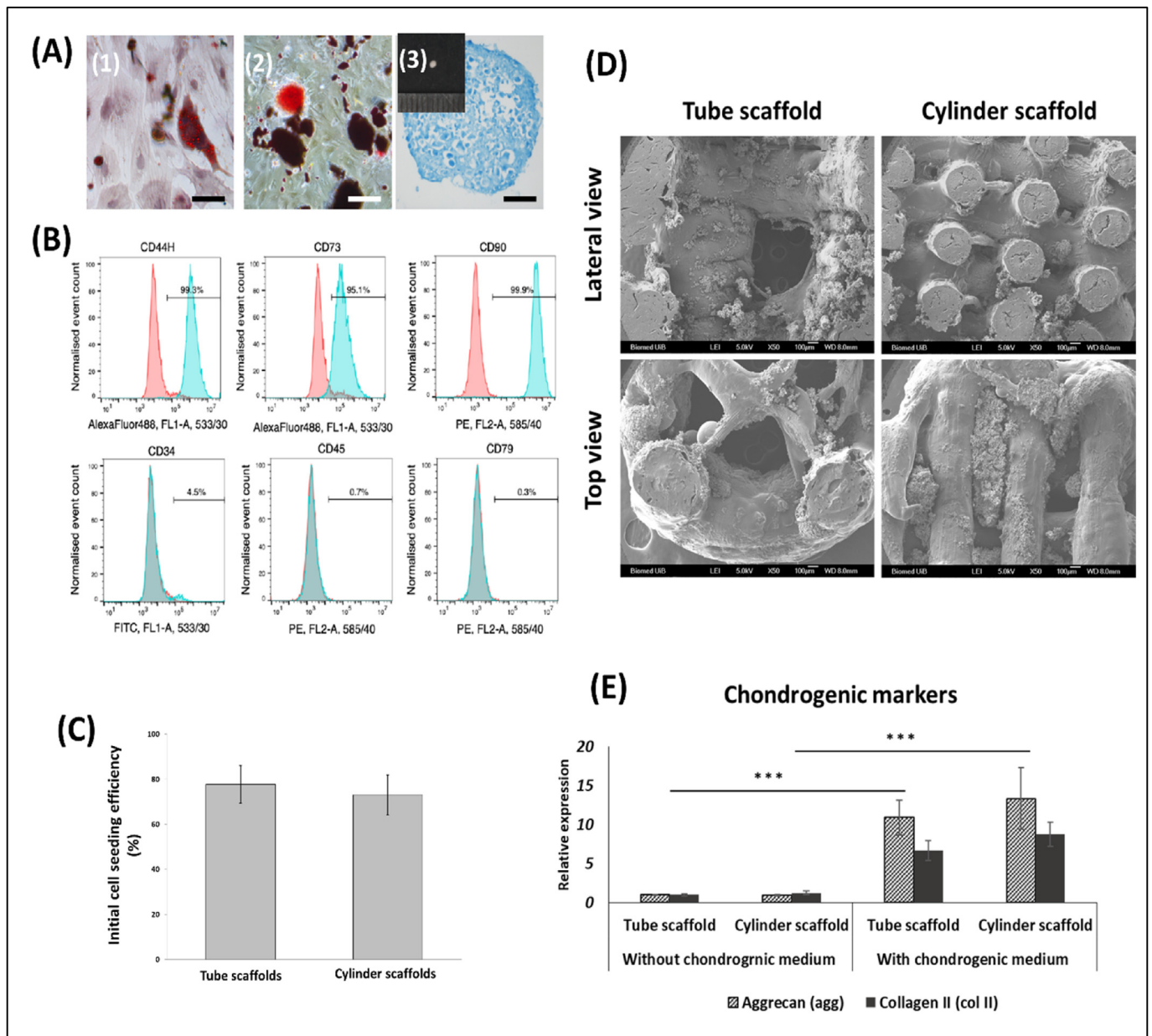
Fig. 3. (**A**) Characterization of rBMSC. Under inductive culture conditions, the cells were able to differentiate into; (1) osteoblasts using Alizarin red staining, (2) adipocytes using Red oil O staining or (3) chondrocytes using Alcian blue staining. (**B**) Analysis by flow cytometry showed that rBMSC exclusively expressed putative rat MSC markers, including CD44H, CD73, and CD90, but did not express hematopoietic markers such as CD34, CD45 and CD79. (**C**) Initial cell attachment efficiency, assessed after 24-h' culture on the scaffolds. The efficiency of the two designs was comparable. (**D**) SEM images after 21 days' induction show that the cells seeded onto the 3D printed scaffolds formed complexes of chondrocyte-like cells. (**E**) To confirm the chondrogenesis in the scaffolds, chondrogenic markers aggrecan (agg) and collagen II (col II) were analyzed using PCR. Agg and col II expressions exhibited significant overall upregulation in relation to condrogenic medium after 21 days (p < 0.001). (For interpretation of the references to color/colour in this figure legend, the reader is referred to the Web version of this article.)

extracellular matrix. The increased expression of AGG and Col II genes among bone marrow derived rat mesenchymal stem cells suggests improved chondrogenic potential, which is consistent with previous findings [42]. The spherical cell morphology of cells seeded onto 3D printed poly(LA-co-CL) scaffolds was observed after 21 days of incubation. This is in agreement with a previous observation of spherical morphology of MSC in 3D cultures [55] which can be related to deposition of extracellular components representative of cartilaginous tissues (Fig. 3B). In endochondral bone tissue engineering applications, the cell source is of great importance: the cells must be able to undergo chondrogenic differentiation, they should produce a cartilaginous matrix and release the pro-angiogenic factors required to facilitate vascularization and bone tissue formation [56]. In early work on bone tissue

regeneration, polymer scaffolds seeded with articular chondrocytes were implanted into calvarial defects. The neo-tissue formed in these constructs was reported to be stable cartilage, resistant to vascularization and ossification [57]. Moreover, on expansion *in vitro*, chondrocytes lose their phenotypic potential [58,59]. On the other hand, MSC have the capability to undergo several population doublings *in vitro*, and the use of chondrocytes pre-differentiated from MSC that isolated from bone marrow [21] or embryonic stem cells [22] have been transplanted to stimulate endochondral bone formation *in vivo* [17]. In addition, following implantation, chondrogenic phenotypes of MSC are dependent on the tissues from which the cells were harvested, with BMSC demonstrating the ability to proceed down the endochondral route following chondrogenic induction [60].
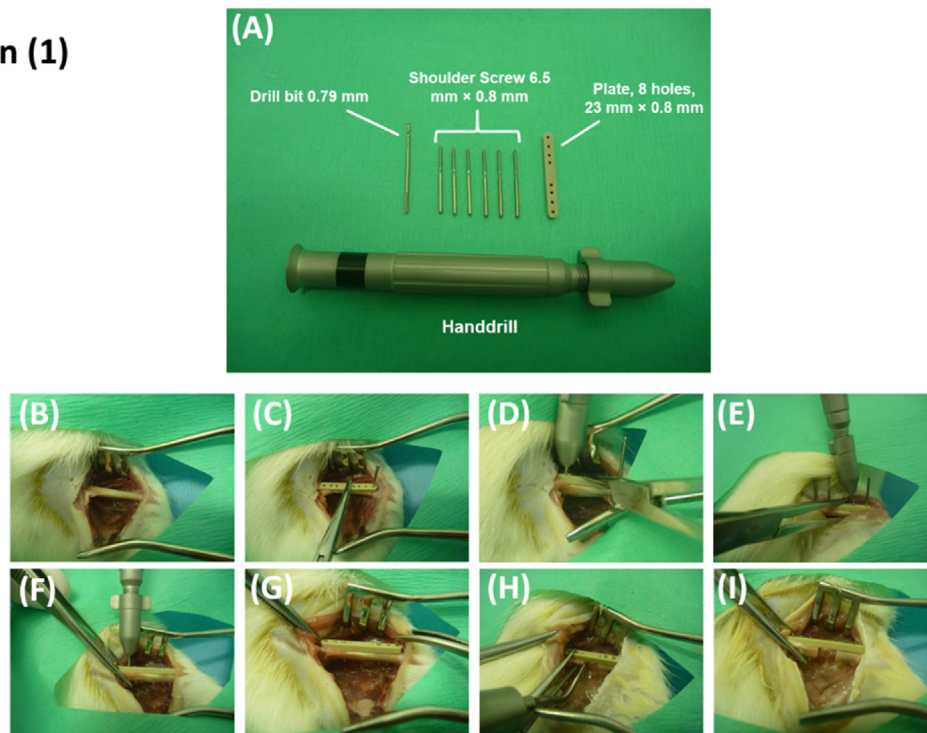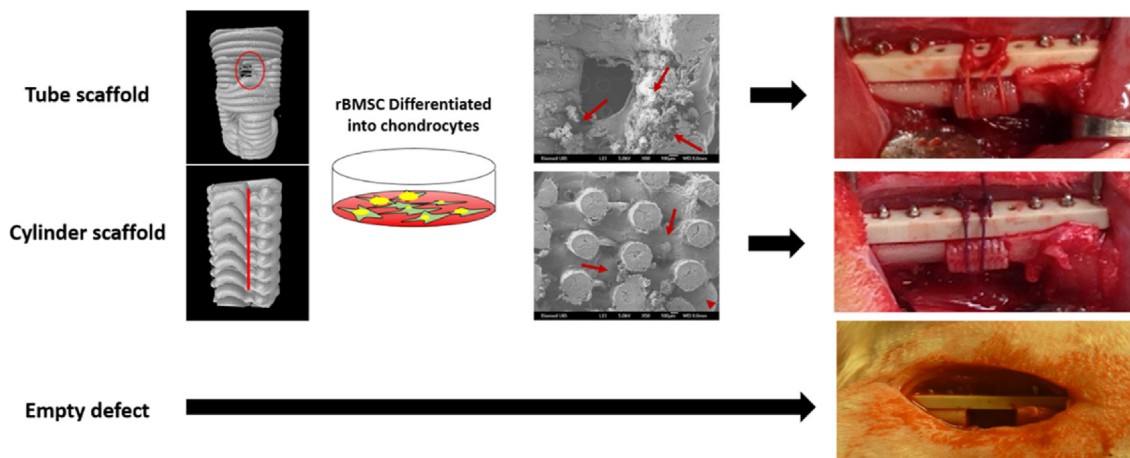
Fig. 4. Section (1): the surgical procedure. (A): the Piezotome Solo (Acteon) used to create a 5 mm femoral defect. The surgical steps are shown from (B) to (I). Section (2): the experimental groups (Tube scaffolds, Cylinder scaffolds and the control) and scaffold implantation.

3.3. Osteogenic metabolic activities of 3D printed constructs

Fig. 4 shows the surgical procedure and implantation of the 3D printed scaffolds. All experimental animals recovered from the surgical procedure and continued in good health. There were no signs of adverse tissue response, severe inflammation or wound healing complications during the observation period of 15 weeks. Moreover, no changes were observed in the behavior of the animals or their normal weight development. Bone formation involves a dynamic interaction of biological activity and dynamic PET/CT imaging is considered an appropriate method for real-time tracking of the rate and extent of bone regeneration. Over the past ten years, [18F]–NaF PET/CT has become widely accepted as the ideal radionuclide imaging technique for investigation of metabolic bone activity [61]. This is due primarily to the superior properties of [18F]–NaF as a bone-seeking tracer and to the better spatial resolution of PET scanners than either planar or single photon emission computed

tomography [62]. The uptake of [18F]NaF is directly proportional to the metabolic activity of osteogenic cells at the defect [62]. Thus, PET/CT was used to detect early bone forming activity at the segmental defect.

To monitor new bone formation in the defects of the left femurs, nanoScan small animal CT scans were acquired at 1, 3, 5, 7, 11 and 14 weeks post operatively (Fig. 5). However, a disadvantage of [18F]–NaF is the short half-life, which currently limits the potential for long-term tracking with a single radiopharmaceutical injection. Consequently, for slow biological processes such as bone regeneration, this radiotracer can be injected periodically (usually weekly) [63]. To follow the progress of bone formation in the defect gap, X-ray computed topography was acquired at intervals *in vivo*, under anesthesia, for all rats in the experimental and the control groups after surgery. The radiolucency of poly(LA-co-CL) scaffolds allowed visualization of the newly formed bone at the defect. At week 1 CT scanning, no apparent new bone formation was observed in any group. At week 3, new bone formation was
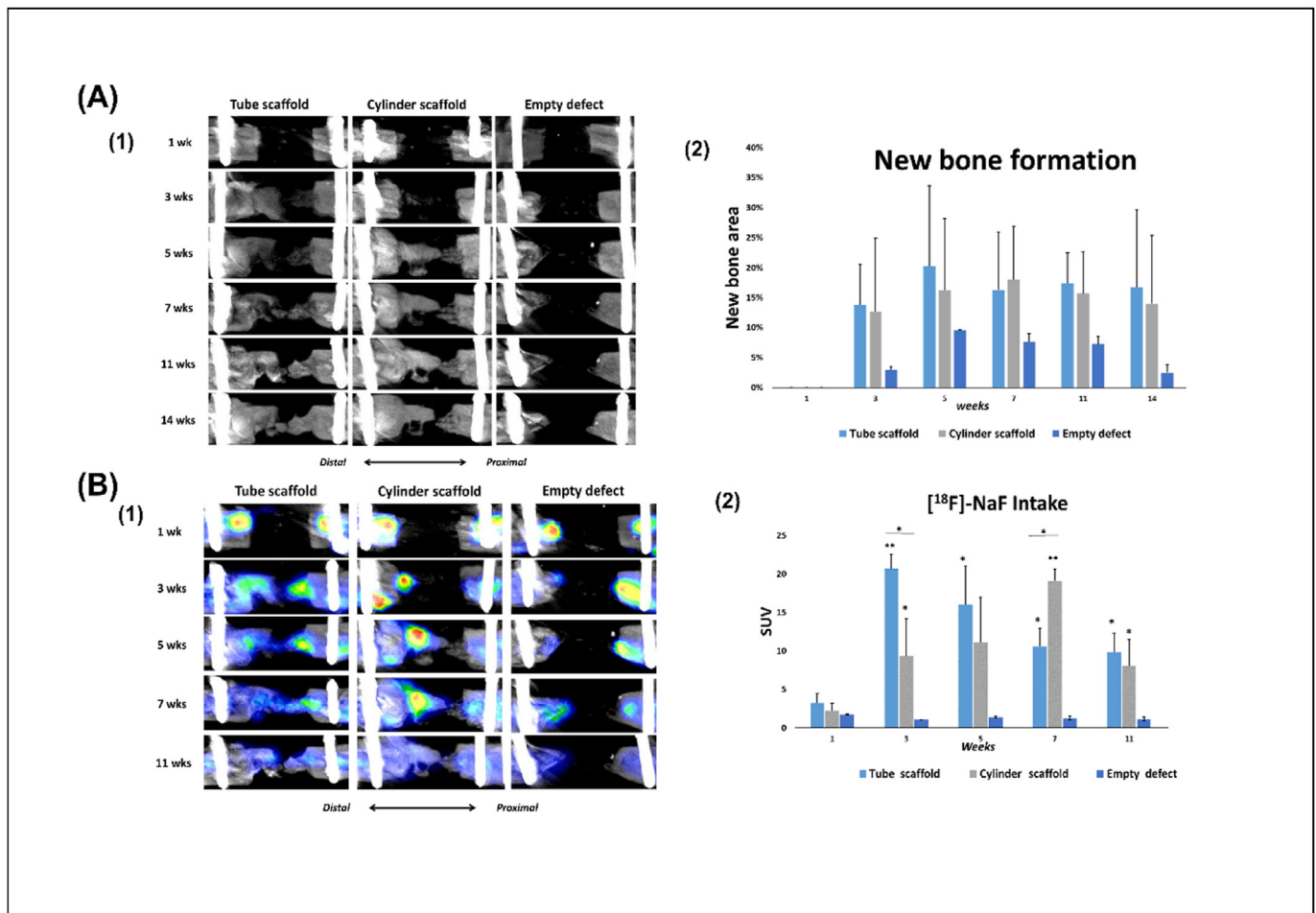
Fig. 5. (A) *In vivo* bone formation analysis (1) Representative *in vivo* femoral x-ray computed topography for rats in all groups at 1, 3, 5, 7, 11 and 14 weeks postoperatively. (2) The bar shows the quantification of the area of new bone formation. At one week postoperatively no area of bone formation was observed. (B) Osteogenic activity assessed by PET/CT. (1) PET/CT reconstructed images show the areas of [18F]-NaF uptake. The PET/CT was done at intervals (1, 3, 5, 7 and 11 weeks postoperatively) (2) Quantification of [18F]NaF uptake by the bone. The mean standardized uptake values (SUVmean) were calculated from VOIs covering the defects. The measurements were made on the same rats (n = 5/per group). Throughout the experimental period, there was a significant difference between the defects treated with 3D printed poly(LA-co-CL) seeded with chondrocyte-like cells and the control group. At week 3, bone metabolic activity was significantly higher in Tube scaffolds than in Cylinder scaffolds. However, at week 7, this difference was reversed, and metabolic activity was significantly higher in Cylinder scaffolds than in the Tube scaffolds. (*: $p < 0.05$, **: $p < 0.01$).

seen in both 3D printed scaffold groups. At weeks 5, 11 and 14, the newly formed bone was larger and showed higher bone density in the Tube scaffolds than in the Cylinder scaffold, but the difference was not significant. New bone growth tended to proceed primarily through the intramedullary canal, which was predominant in Tube scaffolds. However, at week 7, the newly formed bone in the Cylinder scaffolds was larger and denser than in the Tube scaffolds. The empty defects failed to heal, confirming that the 5 mm defect is a critical size in long bone defects in rats.

As a tracer for the bone remodeling marker, ^{18F}–NaF was used for PET examination at 1, 3, 5, 7 and 11 weeks (Fig. 7). At week 1, ^{18F}–NaF uptake was observed at the distal section of the femur and the inserted screws at the proximal section of the femur in all groups. At weeks 3 and 5, significantly greater ^{18F}–NaF uptake was detected at newly formed bone areas in defects treated with Tube scaffolds than in the Cylinder scaffolds ($p < 0.05$) or the empty defects ($p < 0.01$). In contrast, at week 7, significantly greater uptake of ^{18F}–NaF was associated with Cylinder scaffolds than with Tube scaffolds ($p < 0.05$) or empty defects ($p < 0.01$). At week 11, there was no significant difference in ^{18F}–NaF uptake between Tube and Cylinder scaffolds. In general, there was no uptake of ^{18F}–NaF in the empty defects.

Throughout the observation period, the difference in ^{18F}–NaF uptake

in the experimental groups was significantly higher than in the control group. The osteogenic metabolic activity of osteoblasts increases after creation of the defect and falls to baseline levels when healing is complete [64]. Uptake of ^{18F}–NaF by the bone involves the exchange of ^{18F} ions with hydroxyl ions (OH−) on the hydroxyapatite surface, to form fluoroapatite. Because of the rapid blood clearance, a high bone to background ratio is achieved with this imaging agent [65]. The uptake is high in new bone because of the availability of more binding sites, hence increased new bone formation is nearly always associated with increased ^{18F} localization [65]. Accordingly, certain factors influence the visualization of the uptake, such as blood flow and the quantity of new bone formation. This can explain the significant difference between the Tube and Cylinder scaffolds, which facilitated the blood flow at weeks 3 and 5. However, after week 5, Cylinder scaffolds seemed to develop a more appropriate blood flow, increasing osteogenic metabolic activity.

3.3.1. Bone healing assessed at 15 weeks after surgery

The study also assessed the impact of the design of the scaffold, simulating long bone structure, in achieving bone tissue regeneration. These designs were not intended as identical replacements of the missing bone, but rather as microenvironments, conducive to endoochondral regeneration. The 3D images of μ-CT reconstruction (Fig. 6A)
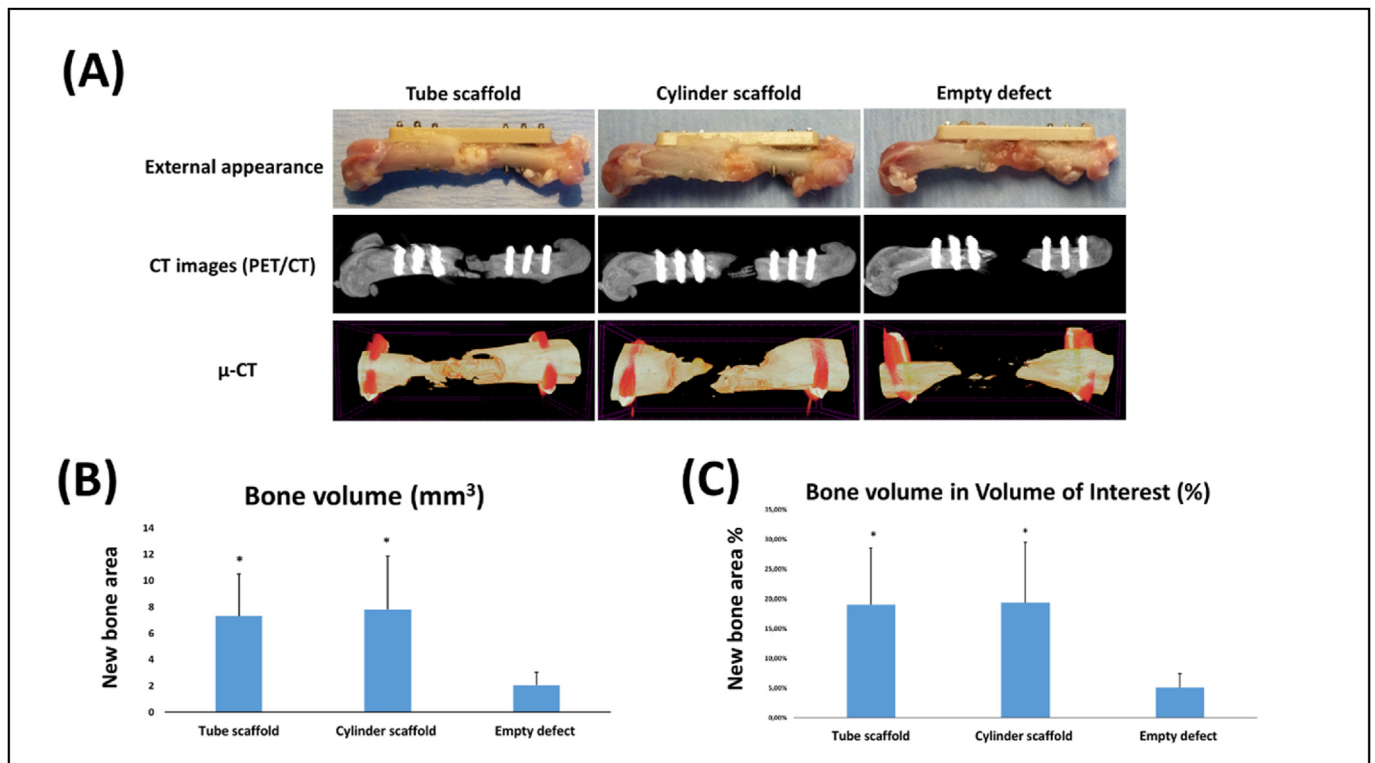
Fig. 6. (A) External appearance, CT images and μ-CT reconstructed images from the two experimental groups and the control at week 15 (; (B and C) μ-CT analysis of new bone formation at week 15 post-implantation: quantitative parameters indicating the new bone formation on various scaffolds based on μ-CT images; bar: 500 μm in (*: $p < 0.05$; n = 10/per experimental group).

demonstrated that in the segmental femoral defect rat model, 3D printed scaffolds seeded with chondrocyte-like cells induce new bone formation within the defects 15 weeks after scaffold implantation. The control (empty defect) remained largely open, with negligible mineralized regions at the center of the defect or on regions confined mostly to the defect edges. As shown in Fig. 6B, at 15 weeks after surgery, the bone volumes (BV) in the Tube (7.32 ± 3.18 mm^3) and Cylinder scaffolds

(7.80 ± 3.18 mm^3) were significantly higher than in the empty defect (2.05 ± 0.97 mm^3) ($p < 0.05$) Moreover, Fig. 6C shows that the percentages of bone volume (BV/TV) were significantly higher in the Tube ($19.01 \pm 9.51\%$) and the Cylinder scaffolds ($19.41 \pm 10.10\%$) than in the empty defects ($5.08 \pm 2.37\%$) ($p < 0.05$). Quantification of the newly formed bone from the μ-CT images, including the bone volume (BV) and bone volume density (bone volume/tissue volume, BV/TV) demonstrates
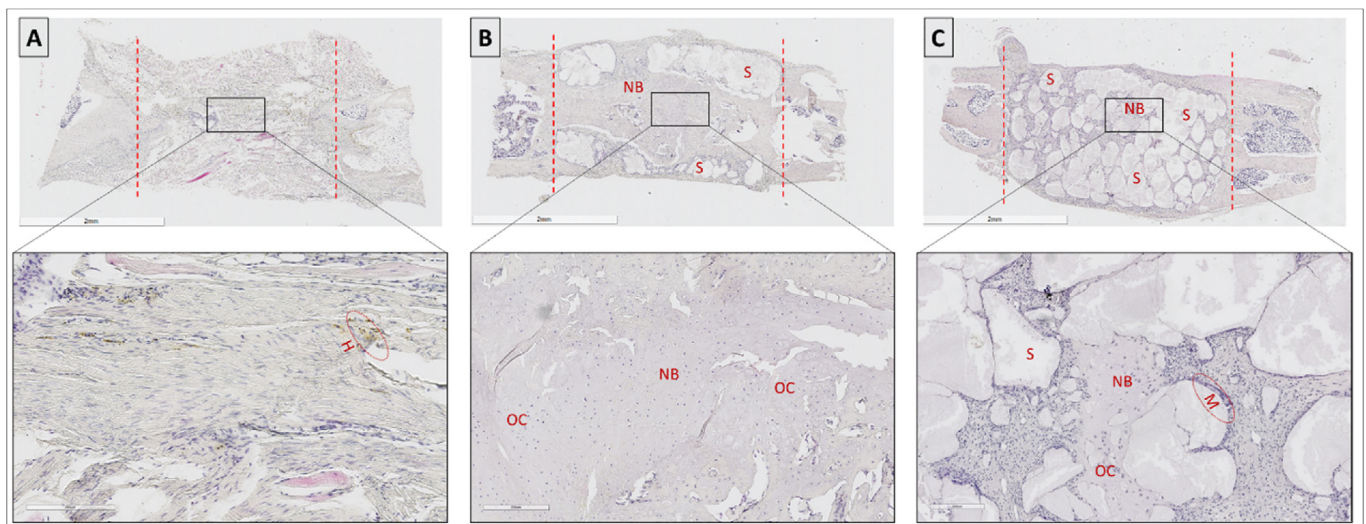

Fig. 7. Histological images after 15 weeks (HE). (A) Empty defect, magnified below, showing the defect filled with connective tissue. (B) Tube scaffold, magnified below, showing new bone (NB) bridging the defect: poly(LA-co-CL) (S) is still detectable within the defects. (C) Cylinder scaffold, magnified below, showing new bone (NB) between the strands of the scaffolds. New bone and osteocytes (OC) could be seen within the lacunae. Some hemosiderin (H) and mononuclear cells (M) were observed. Scale bar for A, B and C is 2 mm and for the magnified images 200 μm.

significant bone tissue formation in defects treated with 3D printed poly(LA-co-CL) porous scaffolds regardless the design comparted to empty defect.

While significantly more bone was deposited in the defects treated with the experimental constructs than in the empty defects, regeneration of the segmental critical-sized defect was persistently incomplete. Long bone defects frequently involve both cortical and cancellous bone, indicating a hierarchical structure with gradient mechanical properties, hence the difficulties involved in regeneration. It is reported that around 64% of *in vivo* studies have been conducted in the cranio-maxillofacial region and 32% in load-bearing sites [66]. Scaffolds in load-bearing defects specifically require adequate mechanical properties. The bone bridge can be seen at the two sides of the 3D scaffolds, which is a typical phenomenon in repair of long bone fracture, due in part to the gradient mechanical stimulation created by the fixation [67]. 3D printed scaffolds might simulate the structure of the native bone tissue according to size and shape. Moreover, using 3D printed scaffolds, constructs can be designed with controlled internal and external architectures, with specific settings [68,69]. In the defects treated with 3D printed scaffolds seeded with chondrogenic differentiated MSC, bone formation was significantly high after 15 weeks. This finding is in accordance with related studies in which hypertrophic chondrocytes [70], differentiated from MSC through *in vitro* culture, improved bone formation compared with undifferentiated MSC [17] or MSC differentiated into osteoblasts [71,72]. Long bone defects present a multifaceted signaling microenvironment, with structural, mechanical and biological factors stimulating repair through endochondral ossification. The great regeneration caused by the chondrocyte-like cells seeded into 3D scaffolds is assumed to be due to the progression of natural ossification of long bone.

The bone formation did not vary significantly between Tube and Cylinder scaffolds. Tube design, however, cause bone to grow in diagonal directions along with a hollow internal structure. Further, in load-bearing bone defect, mechanical properties are very important for tissue regeneration [73]. When structures are stiff enough, they would be able to withstand most pressure, however bone tissue will not be stimulated by stress. Stress is known to promote bone tissue growth and aid bone reconstruction according to literature [74]. On the other hand, too low stiffness would lead to too much loading on bones, resulting in fractures. The current study aimed to design biomimetically constructs for load-bearing bones. Biometric strength was required under stress and torque loads to prevent implants from sliding, loosening, or even breaking after implantation. Comparing the mechanical properties of two designs resulted in comparable bone formation, indicating that the 3D printed scaffolds are isotropic in their mechanical properties in agreement with previous report [75].

Histological staining confirmed that poly(LA-co-CL) scaffolds enhanced bone regeneration (Fig. 7). In the empty defects, connective tissues were found in the region of the bone defect. Moreover, the bone marrow space at the margins of the wound seem to contain fatty connective tissue. In contrast, in the 3D printed scaffold groups, abundant amounts of newly formed bone tissue were detected, not only around the construct but also within the scaffolds, through the interconnecting pores. In the Tube scaffolds, the entire area between the wound margins was filled with new bone and osteocytes could be seen within the lacunae with distinct Haversian systems. As in normal bone marrow, the marrow spaces were also composed of connective tissue, adipocytes, and mostly mononuclear cells, with a few giant cells and neutrophils. Some hemosiderin was observed in the marrow spaces. This indicates bleeding or leaky blood vessels: some of this hemosiderin was engulfed by macrophages, indicating an ongoing "mopping-up" process. For cylinder scaffolds, less bone was detected between the two wound margins. In addition, there was still some marrow spaces that fits the description above. These results further demonstrate that the 3D printed poly(LA-co-CL) scaffolds function as osteoconductive constructs *in vivo*; their osteoconductive properties are further enhanced by seeding with chondrocyte-like cells.

It is common to study bone regeneration by designing scaffolds and matrices but utilizing modalities such as 3D printing for translational research remains underutilized [76]. Scaffold-based bone tissue engineering remains an elusive approach to total reconstruction of large segmental bony defects [77]. 3D printed scaffolds must facilitate new bone growth while eventually degrading, allowing native bone to regain its form and function. However, the polymer material was still detectable 15 weeks after implantation. A longer healing process may be implied by the delayed degradation of the 3D printed poly(LA-co-CL) in this experimental model [36].

4. Conclusions

Reliability and efficacy are two major issues in regeneration of large bone defects, and both were achieved by the techniques described in this study. If the very promising outcomes observed in rodents prove to be reproducible in humans, this could open way to the development of clinical applications of "personalized medicine". In cell-based bone tissue engineering, bone formation can be based on intramembranous or endochondral ossification. 3D printed poly(LA-co-CL) scaffolds were successfully fabricated by a 3D-Bioplotter ® extrusion printer at high temperature. The above data further indicate that bone-healing efficiency was enhanced by endochondral bone regeneration using chondrogenically-induced stem cells seeded into 3D printed scaffolds, and that quantitative PET imaging of bone turnover is appropriate for measuring the metabolic activity of cells. The 3D printed scaffolds, with two different designs, not only exhibited excellent *in vitro* cell material interactions, but similarly also exhibited the ability to stimulate new bone formation through endochondral ossification.

The results of this study are promising. In the rat femur model, tailormade 3D-printed scaffolding seeded with chondrocytes derived from BMSC effectively led to significant endochondral ossification. Moreover, the study presents quantitative and qualitative methods for monitoring the experimental procedure. Further investigation is warranted to determine optimal scaffold design and the application of different stem cells for use in different anatomic sites and indications.

Credit author statement

Kenji Hara: Conceptualization, Methodology, Investigation, Formal analysis, Writing – review & editing. Endre Hellem: Methodology, Writing – review & editing. Shuntaro Yamada: Methodology, Writing – review & editing. Kemal Sariibrahimoglu: Methodology, Writing – review & editing. Anders Mølster: Resources. Nils R Gjerdet: Resources, Writing – review & editing. Sølve Hellem: Resources, Writing – review & editing. Kamal Mustafa: Resources, Supervision, Writing – review & editing, Funding acquisition. Mohammed A. Yassin: Conceptualization, Methodology, Writing – original draft, Formal analysis, Supervision, Investigation.

Declaration of competing interest

The authors declare that they have no known competing financial interests or personal relationships that could have appeared to influence the work reported in this paper.

References

[1] T.A. Einhorn, L.C. Gerstenfeld, Nat. Rev. Rheumatol. 11 (1) (2015) 45.
[2] J.A. Bishop, et al., J. Am. Acad. Orthop. Surg. 20 (5) (2012) 273.

[3] M.A. Flierl, et al., J. Orthop. Surg. Res. 8 (1) (2013) 33.
[4] F.H. Albee, Am. J. Surg. 63 (3) (1944) 421.
[5] E. Gomez-Barrena, et al., J. Cell Mol. Med. 15 (6) (2011) 1266.
[6] A.R. Amini, et al., Crit. Rev. Biomed. Eng. 40 (5) (2012) 363.
[7] F. Shapiro, Eur. Cell. Mater. 15 (2008) 53.
[8] E.M. Thompson, et al., J Tissue Eng Regen Med 9 (8) (2015) 889.
[9] H.M. Kronenberg, Nature 423 (6937) (2003) 332.
[10] C. Yang, et al., Engineered Regeneration 2 (2021) 171.
[11] D. Gawlitta, et al., Tissue Eng. B Rev. 16 (4) (2010) 385.
[12] C.H. Coyle, et al., J. Orthop. Res. : official publication of the Orthopaedic Research Society 27 (6) (2009) 793.
[13] A.R. Armiento, et al., Acta Biomater. 65 (2018) 1.
[14] C. Stüdle, et al., Biomaterials 171 (2018) 219.
[15] K. Pelttari, et al., Arthritis Rheum. 54 (10) (2006) 3254.
[16] P. Janicki, et al., Acta Biomater. 6 (8) (2010) 3292.
[17] J. van der Stok, et al., Eur. Cell. Mater. 2014 (27) (2014) 137.
[18] C.S. Bahney, et al., J. Bone Miner. Res. 29 (5) (2014) 1269.
[19] E. Farrell, et al., Tissue Eng. C Methods 15 (2) (2009) 285.
[20] E. Farrell, et al., BMC Muscoskel. Disord. 12 (1) (2011) 31.
[21] N. Harada, et al., Biomaterials 35 (27) (2014) 7800.
[22] J.M. Jukes, et al., Proc. Natl. Acad. Sci. Unit. States Am. 105 (19) (2008) 6840.
[23] I. Denry, L.T. Kuhn, Dent. Mater. 32 (1) (2016) 43.
[24] V. Mironov, et al., Trends Biotechnol. 21 (4) (2003) 157.
[25] A. Kumar, et al., Mater. Sci. Eng. R Rep. 103 (2016) 1.
[26] H. Ma, et al., Acta Biomater. 79 (2018) 37.
[27] N. Chantarapanich, et al., Computational and Mathematical Methods in Medicine 2012 (2012) 407805.
[28] P. Diloksumpan, et al., Advanced Healthcare Materials 9 (10) (2020) 1901807.
[29] G. Tripathi, B. Basu, Ceram. Int. 38 (1) (2012) 341.
[30] I. Chiulan, et al., Bioengineering (Basel) 5 (1) (2017).
[31] S. Jain, et al., Biomacromolecules 21 (2) (2020) 388.
[32] M.A. Yassin, et al., Macromol. Biosci. (2017) 1600427.
[33] M.A. Yassin, et al., J. Biomed. Mater. Res. 104 (8) (2016) 2049.
[34] S. Suliman, et al., Advanced Healthcare Materials 5 (6) (2016) 730.
[35] Y. Sun, et al., J. Biomed. Mater. Res. 100A (10) (2012) 2739.
[36] M.A. Yassin, et al., J. Biomed. Mater. Res. 103 (11) (2015) 3649.
[37] S. Danmark, et al., Acta Biomater. 7 (5) (2011) 2035.
[38] S. Dånmark, et al., J. Bioact. Compat Polym. 25 (2) (2010) 207.
[39] M.E. Broz, et al., Biomaterials 24 (23) (2003) 4181.
[40] J. Fernández, et al., J. Mech. Behav. Biomed. Mater. 9 (2012) 100.
[41] S. Yamada, et al., J. Tissue Eng. 12 (2021), 20417314211019375.
[42] N. Bhardwaj, S.C. Kundu, Biomaterials 33 (10) (2012) 2848.
[43] S.M. Bittner, et al., Acta Biomater. 90 (2019) 37.
[44] L.G. Bracaglia, et al., Acta Biomater. 56 (2017) 3.
[45] S.M. Bittner, et al., Mater. Today 21 (8) (2018) 861.
[46] Y. Lai, et al., Biomaterials 153 (2018) 1.
[47] C. Perier-Metz, et al., Biomech. Model. Mechanobiol. 20 (5) (2021) 1723.
[48] L. Roseti, et al., Mater. Sci. Eng. C 78 (2017) 1246.
[49] A. Di Luca, et al., Biofabrication 8 (4) (2016), 045007.
[50] X.H. Xie, et al., J Tissue Eng Regen Med 9 (8) (2015) 961.
[51] J.I. Huang, et al., JBJS 88 (4) (2006) 744.
[52] J.M. Sobral, et al., Acta Biomater. 7 (3) (2011) 1009.
[53] D.P. Byrne, et al., Biomaterials 28 (36) (2007) 5544.
[54] S. Jain, et al., Biomacromolecules (2019).
[55] R. Seda Tigli, et al., Journal of tissue engineering and regenerative medicine 3 (5) (2009) 348.
[56] E.J. Sheehy, et al., Materials Today Bio 3 (2019) 100009.
[57] W.S. Kim, et al., Plast. Reconstr. Surg. 94 (5) (1994) 580.
[58] A. Barbero, et al., Osteoarthritis Cartilage 12 (6) (2004) 476.
[59] J. Diaz-Romero, et al., J. Cell. Physiol. 202 (3) (2005) 731.
[60] Tissue Eng. 18 (11–12) (2012) 1161.
[61] W. Raynor, et al., Curr. Osteoporos. Rep. 14 (4) (2016) 115.
[62] P.S. Lienemann, et al., Sci. Rep. 5 (2015) 10238.
[63] E.A. Fragogeorgi, et al., J. Tissue Eng. 10 (2019), 2041731419854586.
[64] C.M. Cowan, et al., Nat. Biotechnol. 22 (5) (2004) 560.
[65] A.J. Timmermans, et al., European Journal of Hybrid Imaging 3 (1) (2019) 18.
[66] C. Garot, et al., Adv. Funct. Mater. 31 (5) (2021) 2006967.
[67] M. Bottlang, F. Feist, J. Orthop. Trauma 25 (Suppl 1) (2011) S21.
[68] S.V. Murphy, A. Atala, Nat. Biotechnol. 32 (8) (2014) 773.
[69] A.C. Daly, et al., Adv Healthc Mater 6 (22) (2017).
[70] Y. Liu, et al., Biomaterials 218 (2019) 119336.
[71] E.M. Thompson, et al., Tissue Eng. 22 (5–6) (2016) 556.
[72] J. Bernhard, et al., Biomaterials 139 (2017) 202.
[73] Y. Zhang, et al., Regenerative Biomaterials 4 (2) (2016) 81.
[74] F. Naddeo, et al., Compos. B Eng. 115 (2017) 60.
[75] B. Zhang, et al., Mater. Des. 152 (2018) 30.
[76] L. Witek, et al., J. Orthop. Res. 37 (12) (2019) 2499.
[77] Y. Kinoshita, H. Maeda, Sci. World J. (2013) 2013.